Structural assessment and material validation of 3D printed corrugated spacecraft debris shields

Adrian Dumitrescu[(1)], Scott J. I. Walker[(2)], Federico Romei[(3)], Atul Bhaskar[(4)]

[(1)] *University of Southampton; University Road, Southampton, SO17 1BJ, UK; ad2g15@soton.ac.uk*
[(2)] *University of Southampton; University Road, Southampton, SO17 1BJ, UK; sjiw@soton.ac.uk*
[(3)] *University of Southampton; University Road, Southampton, SO17 1BJ, UK; f.romei@soton.ac.uk*
[(4)] *University of Southampton; University Road, Southampton, SO17 1BJ, UK; a.bhaskar@soton.ac.uk*

KEYWORDS: Additive Manufacturing, 3D Printing, Satellite Shielding, Satellite Structures, Hypervelocity Impact, ReDSHIFT

ABSTRACT

In the context of novel and lighter satellite designs, this paper investigates a 3D printing approach to the standard satellite orbital debris shields. Shields are currently produced using conventional manufacturing techniques and are limited in terms of design variation. 3D printing can lead to a wider range of more optimized shield designs that are easier and faster to fabricate compared with standard samples. Moreover, metal printing may enable the shields to augment and support the primary structure of the satellite in its load bearing functions.

The objective of this paper is to present a structural and shielding assessment of AlSi10Mg 3D printed single corrugated orbital debris shields based on experimental data generated from 6 static structural samples and 8 hypervelocity impact (HVI) samples manufactured and tested during the ReDSHIFT project. The samples were subjected to three point bending (3PB), compression and HVI - the three loading scenarios relevant for both structural and shielding purposes. Experimental results from testing of these novel structures are compared with those for baseline structures to gain insight into the structural value of the proposed novel shields and into their protection capabilities. Finally, the experimental results are compared with those from Finite Element Analysis (FEA) carried out within the ANSYS APDL 2020 environment (bending and compression) and Smooth Particle Hydrodynamics (SPH) analysis in AUTODYN (HVI). The use of relevant theory is made to interpret and explain the results. A material model for printed AlSi10Mg is validated and can be used in the development of such novel corrugated shields that have the potential of playing a structural role.

1 INTRODUCTION

Satellite shields have evolved from a slab of material to the first mention of the Whipple shield in 1947[1] to a variety of shield types that take advantage of the separation between multiple shield elements. The common shield types used and investigated today are described below based on the work of Cour-Palais, Chrstiansen and Kerr[2][3][4][5].

Single sheet monolithic Shield - the most rudimentary type of shielding and the least mass efficient. Its Ballistic Limit Equation (BLE) is not dependent on the velocity regime as that dependence relates to the debris that hits the rear wall, which is non-existent here.

Whipple Shield - the first deviation from the single sheet monolithic shield. Note that it is less effective at low impact velocities (same behaviour as a single sheet < 3 km/s) and at certain oblique impact angles at high speeds. These kinds of impacts result in solid and more penetrating fragments that hit the rear wall.

Stuffed Whipple (SW) Shield - a standard Whipple shield that incorporates a blanket of Nextel and Kevlar between its usual layers. The Nextel cloth generates higher shock pressures and greater disruption of the projectile compared to an equivalent weight Aluminium (Al) bumper. The Kevlar slows down the remaining fragments more effectively than Al due to its high strength to weight ratio.

Multi-Shock (MS) Shield - a low-weight shielding alternative to the Whipple shield. It is made up of multiple ultra-thin space sheets usually made out of Nextel. It has been proven to be more efficient than Whipple shields at breaking up projectiles, converting projectile kinetic energy into internal energy of projectile fragments and decreasing the velocity of the debris cloud impacting the rear wall.

Mesh Double-Bumper (MDB) Shield - advanced design that provides similar protection and weight saving benefits to the MS shield. It is a Whipple shield with an added Aluminium mesh before the bumper and a high-strength fabric layer in front of the rear wall.

The performance of these shields has been thoroughly

Proc. 8th European Conference on Space Debris (virtual), Darmstadt, Germany, 20–23 April 2021, published by the ESA Space Debris Office
Ed. T. Flohrer, S. Lemmens & F. Schmitz, (http://conference.sdo.esoc.esa.int, May 2021)

tested and in general Whipple shields outperform monolithic shields, while multi-bumper shields such as MS and MDB offer improvements over standard Whipple shields in several areas.

1.1 Corrugated Shields

A less common, but very efficient shield type is the corrugated shield which so far has been produced through subtractive manufacturing techniques. Work on space debris shields with corrugated cores has accelerated in the past few years, but this type of shield design has been around for more than 30 years. In 1991, Schonberg and Tullos[6] proposed a dual-wall system with a corrugated bumper and compared it to dual-wall shields with monolithic bumpers. The corrugated shield proved to be significantly more effective in protecting the rear wall both from penetration and spall compared to the classic Whipple configuration. The same investigation yielded an approach to determine the optimal corrugation angle for minimum secondary impacts caused by debris ricocheting off of the corrugations.

More recently, the potential of corrugated shields was reiterated through a numerical simulation study concerned with the comparison between Whipple shields and corrugated shields stuffed (SCS) with epoxy[7]. The simulation accuracy was verified both by comparing it to previous experiments on Whipple shields and by comparing it to a modified version of the Cour-Palais BLEs for double-wall structures[8]. The investigation concluded that the SCS absorbs more energy and disperses the debris cloud more than a Whipple structure of equal mass.

1.2 Performance of Sandwich Panels

Looking beyond purpose-built space debris shields, research has also focused on the impact dispersion properties of sandwich panels with Aluminium honeycomb cores. This is because such structural configurations make up a large portion of the spacecraft primary structure and they will inadvertently be exposed to debris impact. In the context of this research, the behaviour of sandwich constructions is relevant as they act as a performance baseline for the novel corrugated shields in both impact and static loading.

The effect of a hypervelocity impact on sandwich panels with honeycomb cores has been investigated theoretically and using extensive testing for over 50 years. The consensus is that honeycombs exhibit a phenomena called *channeling* which leads to an inferior performance compared with a standard Whipple shield (which is effectively a sandwich panel without a core). *Channeling* refers to the impact kinetic energy being refrained from dispersing across a large area due to the honeycomb cell walls, which leads to higher areal damage on the rear facesheet (or the rear wall in a Whipple shield)[9]. In the case of an Aluminium 6061-T6 honeycomb cell and a Cadmium projectile as well as a Cadmium facesheet, the addition of the honeycomb results in an increase by at least a factor of 3.8 in the rear facesheet thickness required to prevent failure[10]. There are a few experimental exceptions that contradict this conclusion, a notable one being a test campaign by NASA MSFC from 1970 which showed an improved shielding performance for the honeycomb structures[11]. They mentioned the loss of kinetic energy in secondary impacts with cell walls as a potential explanation for this unexpected result.

1.3 The ReDSHIFT Investigation

ReDSHIFT was a Horizon 2020 EU funded project that ran between 2016 and 2019 and brought together several academic and industrial institutions including the University of Southampton[12]. Part of the project focus was on the novel assessment of the mechanical and impact performance of AlSi10Mg 3D printed corrugated shields. Single corrugated panels (SCP) were investigated both in 3PB and compression and were impact tested together with a set of three printed multi-shock panels. 6 static structural samples and 8 HVI samples were tested and modeled using theory and simulation.

The performance of the corrugated shields is compared with that of baseline structures, both in 3PB/compression and impact. CFRP sandwich panels with both standard and printed cores are used as the element of comparison in 3PB and compression, since they have been investigated in a previous paper by the present authors[13]. A 3D printed MultiShock Panel (MSP) together with a standard CFRP sandwich panel are used as baselines in impact and are studied in this paper. These comparisons help gain insight into the performance potential of 3D printed corrugated shields, both in terms of debris protection and structural support.

2 EXPERIMENTAL RESULTS

The sample types investigated in 3PB, compression and HVI are shown in Figures 1 and 2 and their geometrical features are presented in Tables 1 and 2. The SCPs tested in 3PB and compression all have the same corrugation geometry and a wall thickness of 300 μm. The 3PB sample free span is 133 mm.

The SCP impact sample is a single corrugation with 4 different configurations, varying both the corrugation thickness and the core depth. See Figure 2 and note that the facesheets are printed together with the core.

The baseline samples for bending and compression tests are as follows. Firstly, a standard Al 5056 Hexcel honeycomb core sandwich panel with a cell size of 4.8 mm and wall thickness of 18 μm for an apparent core density of 32 kg/m^3. Secondly, a sandwich panel with an AlSi10Mg printed core with a cell size of 4.8 mm and wall thickness of 0.3 mm like most of the shields [13].

Sample Type	Corrugation Dimensions	Sample Dimensions	# Samples	Name
Single Corrugated Panel	Angle: 45^0 Height: 6.87 mm Width: 13.33 mm	Wall thickness: 0.3 mm throughout 3PB: 177 mm × 66.9 mm × 6.87 mm Comp: 80 mm × 80 mm × 6.87 mm	3 3PB 3 Comp	S1B 1 - 3 S1C 1 - 3

Table 1: Main properties of 3PB and compression experimental samples

Sample Type	Sample Dimensions	# Samples	Name
Multi-Shock Panel	Wall Thickness: 0.5 mm throughout Total Depth: 10 or 20 mm	10 mm depth: 1 20 mm depth: 2	MSP 10 MSP 20
Single Corrugated Panel	Facesheet Thickness: 0.5 mm Corrugation Thickness: 0.3 mm or 0.7 mm Total Depth: 10 mm or 20 mm	10 mm depth/0.3 mm t_{wc}: 2 10 mm depth/0.7 mm t_{wc}: 1 20 mm depth/0.3 mm t_{wc}: 1 20 mm depth/0.7 mm t_{wc}: 1	SCP 10 0.3 SCP 10 0.7 SCP 20 0.3 SCP 20 0.7

Table 2: Main properties of HVI experimental samples. Here t_{wc} is the corrugation wall thickness

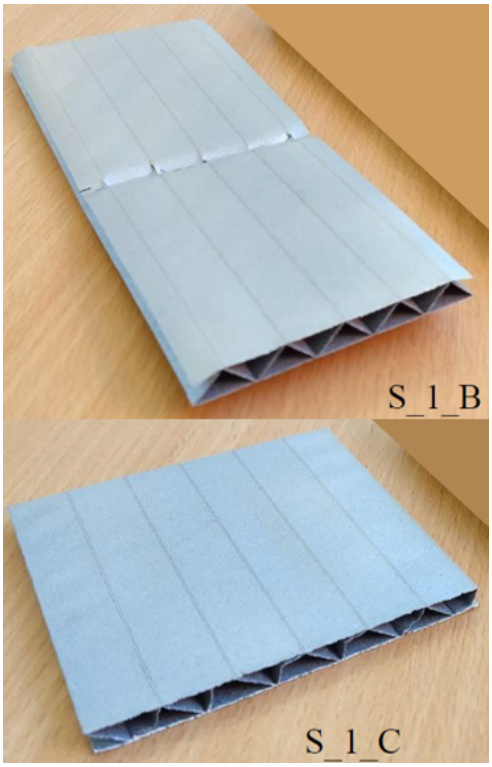

Figure 1: 3D printed shield samples used for 3PB (top) and compression (bottom)[14]

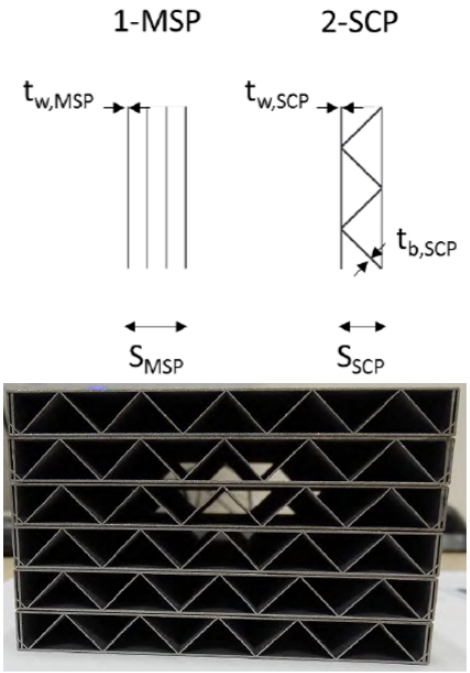

Figure 2: Shield types for impact investigation. Six individual printed single corrugated shields in the bottom figure [15].

The baseline shield is a 3D printed MSP with two core depths. Samples with both 10 mm and 20 mm core depths have 4 walls of 0.5 mm thickness each. Honeycomb cores of various core properties are also used as theoretical comparisons.

All 3PB and compression tests were performed on INSTRON test machines, INSTRON 5560 for 3PB and INSTRON 4204 for compression. The failure load was reported from the INSTRON load cells with sampling every 0.1 second. Displacement was captured using image tracking in ImageJ with a frame every 0.2 - 1 second. The displacement reported by INSTRON can be inaccurate because it includes the displacement of the machine itself, while point tracking isolates the sample displacement. In terms of load peaks, the INSTRON data points assigned to each image frame have a lower sampling rate compared to the raw INSTRON data which will report the true peaks. Two types of error bars will be reported. One of them shows the variation in load or displacement for similar samples undergoing the same loading scenario. The second shows the displacement variation between several points tracked on the same sample. The latter is used to confirm that point tracking was done at reliable and robust locations such as at the cross-head and the supports where virtually no body displacements occur.

The impact experiments were performed at the CISAS HVI Facility using a two-stage Light-Gas Gun (LGG) that can accelerate projectiles of mass up to 100 mg at a top speed of 6 km/s. For this research, Al-1100 spheres from 1.5 mm to 2.9 mm were launched at velocities between 3 km/s - 5 km/s at a normal angle[15].

2.1 Three Point Bending

The 3PB samples are listed in Table 1 and their denominations are S1B 1-3. *S* stands for shield, *B* for bending and *1-3* for the number of the printed specimen. They are the same in compression with *C* instead of *B*.

For these experiments, the point of interest is the sample behaviour before failure and the overall stiffness and strength information obtained from the force - displacement curve. The experimental results reported in Table 3 are averaged across the 3 samples of the single corrugated shield.

Force displacement curves were obtained for all samples and the experimental average as well as the data for all specimens is shown in Figure 3. The averaged peak location is slightly different from what is reported in Table 3 because the imaging force data is used instead of the Instron data. Moreover, samples of the same type have a different displacement at failure, so the peak load of one sample will be averaged with off-peak loads from the other samples for the same displacement.

For all three specimens, the elastic part of the curve is close to linear and does not exhibit the step jumps showed by a sandwich panel with a printed honeycomb core as observed previously in [13].

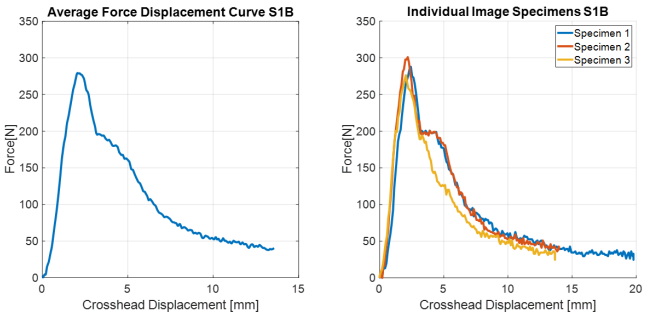

Figure 3: Average force displacement curve for the shields in 3PB (left) and detailed curves for each specimen (right). Imaging data only.

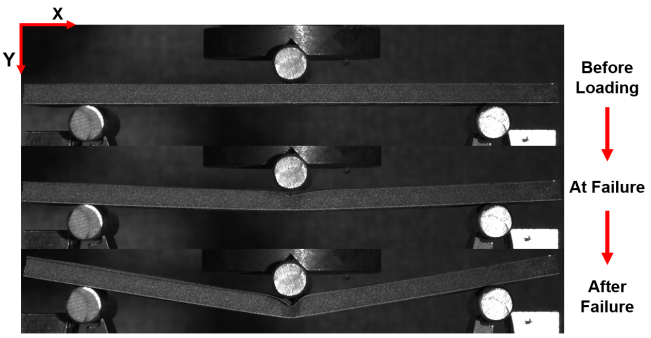

Figure 4: Sequential failure of sample S1B1 represented by Specimen 1 in the graph on the right of Figure 3

Sample	Failure Load (N)	Sample error (N)	Y displacement at failure (mm)	Sample error (mm)	Image error (mm)
S1B	291.3121	-13.983 +13.516	2.2224	-0.1737 +0.2049	±0.0433

Table 3: Experimental results for 3PB

The only small jump indicative of a sequential failure of the sample occurs for specimen 3, but it is much less pronounced compared with the honeycombs from [13]. All S1B samples show a steep decrease in the load applied after failure, denoting a clear 3PB loading peak. The consistency in the force displacement curves of all three samples gives confidence in the robustness of the 3PB behaviour of this type of shield. A representative failure sequence of this shield type is shown in Figure 4.

The mass of the samples was recorded to produce specific values which can then be compared to the results obtained for the baseline honeycomb structures[13]. Note that *HSNB* stands for a standard honeycomb core sandwich panel and *HA0B* stands for a sandwich panel with CFRP facesheets and a 3D printed core. *HSNC* and *HA0C* stand for the same, but in compression.

Sample	Average sample weight (g)	Sample stiffness (N/mm)	Sample specific stiffness (N/(mm×g))
S1B	15.95	131.07996	8.21818
HSNB	41.13	1827.304	44.42752
HA0B	78.72	4541.178	57.6877

Table 4: Mass and stiffness of 3PB shield samples. Honeycomb data added for completion[13].

Based on data in Table 4, the simple corrugation is significantly outperformed by both honeycomb cores. Even the worst performing honeycomb structure, the standard HSNB, has a specific stiffness roughly 5 times that of the best S1B specimen. This is expected since CFRP sandwich constructions with honeycomb cores are very effective in out-of-plane loading. The sandwich panel with a printed core (HA0B) outperforms both the printed shields and the standard core.

These results indicate that integrating corrugated shields with honeycomb primary structures may lead to an overall lower specific stiffness of the structure. However, note that the shields are entirely printed and feature no CFRP face sheets. It would also be useful to compare the two types of core geometry while having similar facesheet properties.

2.2 Compression

The compression samples are listed in Table 1. Results are reported in the same way as before. The buckling load and displacement at failure under compression are presented below in Table 5.

The relative movement of the support affected the vertical displacement results. A relatively small sample error of about ± 0.05 mm becomes significant because the average absolute displacement value is of the same magnitude. In spite of these experimental difficulties, the displacement data for S1C samples is relatively consistent and displacement at failure varies by only 28% between the extremes. Strength was measured more reliably and the variation was of 23% between the highest and lowest buckling load.

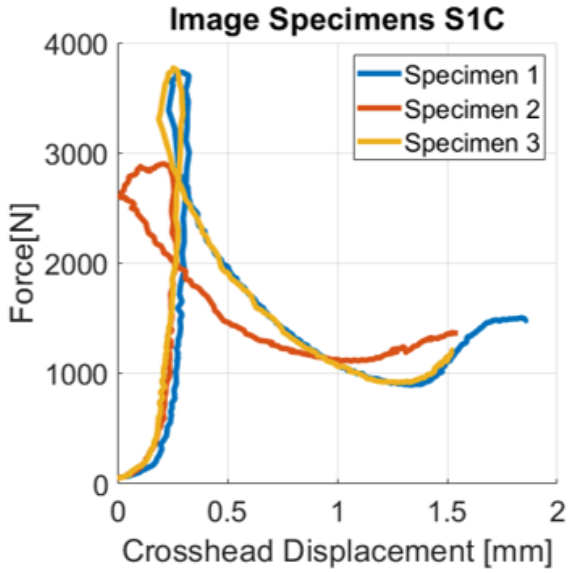

Figure 5: Force - displacement curves for S1C samples. Imaging data only.

The force - displacement curves look similar to those for honeycombs under compression[13] since they have common sources of experimental error such as significant relative movement of the sample support.

Sample	Buckling Load (N)	Sample error (N)	Y displacement at failure (mm)	Sample error (mm)	Image error (mm)
S1C	3481.8399	-570.46 +303.16	0.2528567	-0.04 +0.041	±0.0519

Table 5: Experimental results for compression

Force-displacement plots, obtained from Instron machines, have smooth curves up to the peak, while the imaging plots presented in Figure 5 feature regions where the curve crosses itself as displacement decreases instead of increasing. While the data might seem unreliable, it can be observed that the curves do behave similarly showing consistency in their experimental behaviour.

There is also a geometrical aspect which can explain the displacement trend observed. For all shields, the corrugations make a 45^0 angle with the facesheets. When compressed, the shields naturally want to maintain that inclination with respect to the facesheets. As a result, as the corrugations get more compressed and this angle becomes smaller, the top and bottom faces will deflect upwards and downwards respectively, in an attempt to maintain the 45^0 angle. This results in a cubic deflection of the top and bottom surfaces between every two vertices. This geometrical aspect coupled with the non-ideal experimental setup makes the shield facesheets slightly deflect in the opposite direction to what was expected and this might partly account for the unusual force - displacement curves.

To observe this phenomenon, two types of compression can be simulated. The first, where the application of load over the top facesheet does not constrain the deflection of the top facesheet. The second, done in a similar manner to the experiments and to all simulations in this section, with a block on top of the sample constraining the top face and applying the load. The comparison between the first buckling eigenmode of the two in the case of a diamond core is in Figure 6.

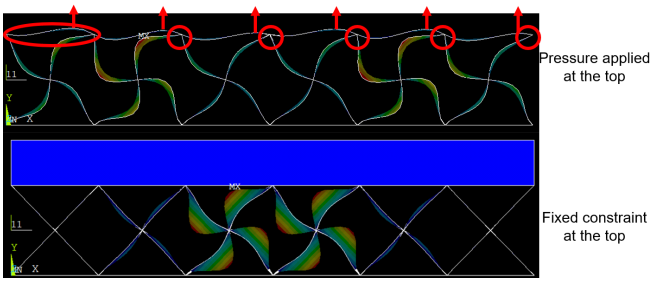

Figure 6: 1^{st} buckling mode. Top figure: the circles show the geometry maintaining the 45^0 angle, the arrows show the top face deflecting up and the ellipse highlights the cubic deflection of the top face.

Overall, the data is robust and once again, the more relevant specific values are evaluated for a better comparison. Based on data reported in Table 6, the performance gap to the honeycomb cores is again evident. Honeycomb sandwich panels are expected to be very stiff in compression and the standard sample (HSNC) has a specific stiffness 4.85 times that of the best performing S1C specimen. When comparing the worst performing standard honeycomb sample to the best performing shield sample, the honeycomb still performs 2.6 times better. Despite having less than ideal displacement data, the difference between corrugations and honeycombs is still quantifiable.

Sample	Average sample weight (g)	Sample stiffness (N/mm)	Sample specific stiffness (N/(mm×g))
S1C	8.75	13770.01242	1573.7157
HSNC	18	150045.4067	8335.856
HA0C	11.09	1093570	98608.72916

Table 6: Mass and stiffness of compression samples. Honeycomb data added for completion[13].

When looking at the 3D printed honeycomb core, the difference in performance increases and further underlines the compromise that would have to be made when integrating shields with spacecraft primary structures. However, some of the loss in mechanical performance due to the integration of the shield is expected to be alleviated by the use of 3D printing, as the AM honeycomb core clearly outperforms its traditional counterpart.

2.3 Hypervelocity Impact

The experimental results for the impact tests have already been reported in a previous paper[15] and the relevant numbers are replicated here. See reference [15] for more details on the experiments and Section 4.3 for the AUDODYN simulation comparison. The experimental setup is in Figure 7.

The main conclusions from experiments ([15] and [16]) are that the 3D printed single corrugated shields (SCP) slightly outperform the baseline printed MSPs. When compared to the theoretical BLE of a same mass honeycomb structure, all 3D printed shields performed significantly better.

Note that more accurate post-processing of the experimental data was done in a ReDSHIFT report[16] such that some results from [15] do not match with the more updated numbers presented in Table 7.

In Table 7, as well as in Table 2, SCP 10 0.3 stands for the single corrugated panel with a 10 mm depth and a 0.3 mm wall thickness, and the rest of the sample names follow the same rule.

Sample	Code	Mean Areal Density (kg/m^2)	Proj D (mm)	Velocity (km/s)	Sample Perforation (Yes/No)	Front Plate Hole Diameter (mm)	Back Plate Hole Equivalent Diameter (mm)
SCP 10 0.3	A03-01	3.97	1.5	4.44	Yes	3.28	8.5
SCP 10 0.3	A03-02	3.97	2.9	4.54	Yes	6	11.7
SCP 10 0.7	A04-01	5.31	1.5	4.84	No	4.3	N/A
MSP 10	A05-01	3.58	1.5	4.49	Yes	2.8	11.7
MSP 20	A06-01	3.5	1.5	4.79	Yes	3	?
MSP 20	A06-02	3.5	2.9	4.6	Yes	4.5	38.8
SCP 20 0.3	A08-01	4.03	1.5	4.7	No	4.1	N/A
SCP 20 0.7	A09-02	5.42	2.9	4.87	Yes	5.9	27.9

Table 7: HVI corrugated shields experimental results from ReDSHIFT[15][16]

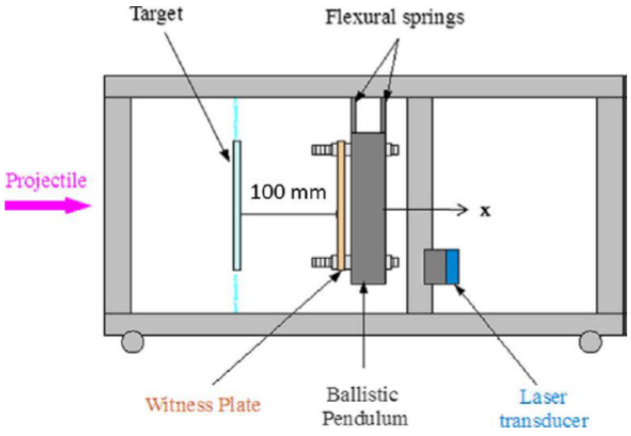

Figure 7: Test setup for the HVI experiments[15]

3 THEORY

The theoretical models that are used as the basis for calculations in this section, are briefly summarized here. Note that due to the thin walls of the printed structures (300 μm) significant porosity was found in all samples. Micromechanics based models had to be used to obtain an accurate value for the apparent Young's Modulus and shear modulus of the printed material. This approach is discussed in [13] and it is also applied here for all material properties used in both theory and simulation.

For the 3PB strength solution, the work by Valdevit, Hutchnison and Evans[17][18] was referred to. It studies both transverse and longitudinal loading of a corrugated core. This approach identifies the main failure modes and provides calculations for the sample failure load for each mode. Note that for transverse loading this work relies on buckling coefficients that stem from the formulas developed by Bazant and Cedolin[19]. For stiffness calculations sandwich beam bending theory is adapted to obtain mid-span deflection.

In compression, the analysis given by Cote[20] relies on the Euler elastic buckling and Shanely[21] plastic bifurcation stresses. It gives the apparent Young's Modulus of both a simple corrugation (S1C) and a diamond core which in turn provides the sample displacement under a compressive load as well as the peak compressive and transverse shear strengths of the corrugated core.

For HVI there is currently no dedicated BLE for corrugated cores and as a result, during ReDSHIFT, scaled versions of existing BLEs were used. They have been mentioned in[15] and are not discussed here.

Based on the theoretical models developed in the papers mentioned, a set of theoretical predictions can be put together for all samples listed in Sections 2.1 and 2.2.

For 3PB the failure load for all failure modes can be obtained and the mode with the lowest predicted load is compared to the experimental result. On the stiffness side, note that the core second moment of area is accounted for in the mid-span displacement bending term because the assumption that the facesheets are significantly stiffer than the core no longer holds. The results for S1B specimens are shown in Table 8.

Sample	Face Yield (N)	Core Yield (N)	Core Yield with Local Indent (N)	Face Buckling (N)	Core Buckling (N)	Core Buckling with Local Indent (N)	Deflection (mm)
S1B	227.16	222.76	157.92	**82.442**	402.95	1937.2	**1.595**

Table 8: Theoretical Predictions for 3PB corrugation samples. Relevant results in bold.

For S1B specimens the failure mode is predicted correctly. Theory predicts face buckling, followed by core yield with local indentation. In real life the failure mode is a combination of the two as can be observed in Figure 3. In 3PB, the theory has qualitative value in predicting experimental outcomes, even for a 3D printed sample with relatively thin walls.

Quantitatively, the theory underpredicts the experimental failure load by 84.5 - 253% for S1B specimens (Face Buckling and Core Yield with Local Indentation values considered). The strength theoretical results rely heavily on assumptions for the corrugation faces end constraints. In longitudinal loading which is relevant for S1B, for buckling, the simply supported boundary condition is used as it is closer to reality. However, it is known that the actual end constraint is between simply supported and fully clamped, so the buckling load will be underpredicted. As a result, it makes sense for theory to underpredict failure loads in 3PB and these results are a confirmation that better understanding is needed regarding the end constraints for this type of structure.

In terms of displacement, the S1B predicted mid-span deflection at failure is underpredicted by 28.3% on average. This relation to the experimental data is expected given that the real samples will have defects.

In compression, given the imperfections and slight asymmetries in the final structure, it is expected that the theory would overpredict the buckling load for all samples. Based on the results in Table 9, on the average, the experimental elastic buckling load is overpredicted by 137%. This is a significant improvement when compared with the predictions for the 3D printed honeycomb from [13]. This can be due to the opposing assumptions regarding core - facesheet interface boundary conditions for the two analyses. For the honeycomb, the core walls constraint was overpredicted as fully clamped, while for the corrugation it is underpredicted as pin jointed. However, even though this boundary condition clearly leads to underprediction compared to the experimental case, the buckling loads are still overpredicted. This is a confirmation of the fact that the effects of sample imperfections, such as pores, on the effective wall thickness are not fully understood and are not accounted for in the theory. All in all, the theory is close to reality both quantitatively and qualitatively, but improvements do need to be made to account for more 3D printed material imperfections.

In terms of sample stiffness, the theoretical shield displacement at the buckling load is significantly underpredicted compared to experimental data.

Sample	Elastic Buckling Load (N)	Deflection at Experimental Failure (mm)
S1C	8267.25	0.01128

Table 9: Theoretical predictions for compression corrugation samples

This is expected because the real samples have important defects including a bottom facesheet that is not perfectly level, while in theory all joins and surfaces are ideal. However, the theoretical results for S1C give a theoretical displacement just 11.2% lower than the simulated value (presented in Section 4.2) which is the more relevant data to compare the theory with. This is a satisfactory outcome which underlines the departure of the experimental setup from the ideal situation.

4 SIMULATION RESULTS

Structural simulations of the shield were performed within ANSYS APDL using Shell 281 elements, for the 3D printed shields and Solid 186 elements for the support and cross-head in 3PB and for the block loading the sample in compression. A friction coefficient of 0.15 was applied between the sample and the support and crosshead in 3PB. For more in depth explanations into how the static FEA models were constructed please refer to [13] since it is concerned with the sandwich panel simulations that were built in the same way as the corrugation models.

4.1 Three Point Bending

A half model was used to simplify the model. Applying symmetry on the X-Y plane (as shown in Figure 8) for a quarter model caused issues so the option was disregarded.

A mesh convergence study was performed with the vertical displacement change being the variable used to assess convergence. The element size of the core faces depends on the corrugation size, while the element size of the corrugation in the transverse direction depends on the element size of the facesheets. The sizes used for the facesheets and the core have to be exact fractions of each other in order for all corrugation end nodes to be merged to the facesheet nodes. The following element sizes are used for S1B after observing that results vary by less than 0.4% when decreasing element size by a further 33%:

- Corrugations: 0.5 mm x 0.83625 mm, where the latter is a 16^{th} of the corrugation width.
- Top/bottom/middle facesheets: 0.5 mm x 2.23 mm, where the latter is a 6^{th} of the corrugation width.

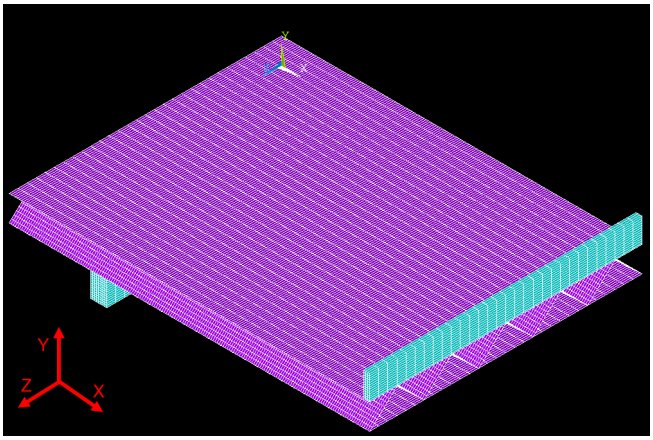

Figure 8: Meshed FEA model of the S1B sample

With the setup shown in Figure 8 the results are:

Sample	Verical displacement (mm)	Sample stiffness (N/mm)	Sample specific stiffness (N/(mm×g))
S1B	1.545	188.551	11.821

Table 10: Simulation results for 3PB shield samples

The simulations underpredict the vertical displacement by 30% at the average experimental failure load. The difference between the theoretical prediction and the simulation result is around 3% which shows good consistency between the two idealized calculations and gives confidence in being able to scale simulation results reliably and predict future experimental outcomes for this type of structure. The variation between FEA and reality can be down to multiple factors including the perfect bonds in the simulated part, the imperfections of the printed part and the complex effects of porosity on sample failure.

4.2 Compression

As the compression samples are smaller and not very computationally intensive, the full model was used instead of a half or a quarter model. The element size dependency on various sample dimensions is the same as before. A mesh convergence study showed that both the buckling load and the vertical displacement change by less than 0.1% when decreasing the element sizes listed below by 50%:

- Corrugations: 1.111 mm which represents a 12^{th} of the corrugation width.
- Top/bottom/middle facesheets: 1.111 mm x 1.666 mm, the two representing a 12^{th} and an 8^{th} of the corrugation width.

The results with this setup can be seen in Table 11. The buckling load predicted by simulations is 3.65 times higher than the experimental results. As with all printed samples, there are significant local imperfections and global asymmetries which lower the experimental buckling load, which means that the simulation results are as expected. Sample height and boundary conditions of the ends of the free sections ultimately determine the buckling behavior of the sample. In the FEA model the vertex where the corrugated sections meet the facesheets gives perfect support to the core members, while in real life that might not be the case due printing faults.

Sample	Elastic Buckling Load (N)	Vertical Displacement at Experimental Buckling (mm)
S1C	12705.5	0.0127

Table 11: Simulation results for compression shields

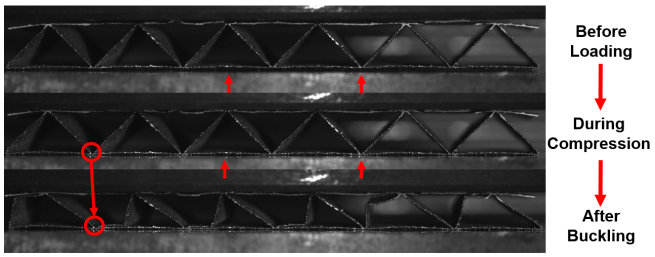

Figure 9: Failure of a S1C sample. During compression the sample support deflects up towards the sample and as the sample fails, it also slides laterally on the support.

In terms of sample displacement at the experimental buckling load, S1C is 20 times stiffer than its experimental counterparts. S1C transmits the loads from the volume pressing on the sample to the corrugated faces that press on the bottom face which is in contact with the support, giving a very stiff setup in an ideal situation. However, there are many factors affecting the displacement data: moving fixtures, the samples sliding and sample asymmetries. Put together they significantly increase the sample displacement at failure as seen in

Figure 9 where sample imperfections are clearly visible especially close to the edges.

All in all, the compression model offers a good comparison to both theory and experiments and it outlines the geometrical aspects that lead to the discrepancies observed.

4.3 Hypervelocity Impact

Hypervelocity impacts depart significantly from the quasi-static loading scenarios investigated up to this point, so a different method is needed to build the simulation models and the new setup is described here.

4.3.1 Software and Computational Method

AUTODYN was chosen as the simulation software since it is the most frequently used and reliable commercially available software. For this research it was accessed through the ANSYS WorkBench package. The computation technique is also different from standard FE codes which split the parts in a mesh which can cause issues when dealing with situations where large deformations are involved. The main problems are mesh tangling and distortion which then lead to the need for unphysical erosion algorithms to delete the problematic mesh elements. The method used to bypass these issues and the need for a numerical grid to calculate spatial derivatives is the smoothed particle hydrodynamic (SPH) technique. It is a meshless Lagrangian technique that was first proposed in 1977 for applications in astrophysics and has since developed into a mature way to deal with impact problems[22].

4.3.2 Impact Location

When using standard Whipple shields, the impact location across the shield is irrelevant because the shield has the same properties throughout. When corrugations are included, the impact changes when the strike location along the corrugation wall changes. There are three main impact locations to consider: the top, middle and bottom of the corrugated geometry. When the impactor hits the top of the corrugation, it will lose more energy in the initial impact, but it will encounter fewer individual impacts across the shield depth which may be detrimental. When it hits in the middle, the number of individual impacts is maximized. When it hits the bottom, the impactor is allowed to disperse more after the initial facesheet contact, but the number of individual impacts is once again at a minimum.

Photos taken during the impact event are available for most experimental samples such that the approximate impact location can be determined. For all shields that contain corrugations, simulations are run for all three impact locations to validate the models used. This also has an effect on the symmetry of the problem because the top and bottom impacts are symmetric across 2 planes (XZ and XY), while the middle impact is only symmetric across the XY plane. See Figure 10 for axes.

4.3.3 Reducing Computational Time

Due to the fact that the corrugations have to be modelled accurately to be able to replicate the experimental results, 3D models are needed. Axisymmetry does not apply to corrugated geometries so 2D models cannot be considered. In order to minimize the computational time, SPH particles are used only in the projectile and in the shield sections that are directly in the path of the projectile, while Lagrangian volume elements are used away from the impact zone. The back facesheet is also made up of Lagrangian volume elements in order to model its deformation more accurately. Moreover, either a quarter or a half model is used depending on impact location and what symmetries apply.

In terms of element size, it is advisable to use around 10 SPH particles per facesheet thickness[23]. Keeping computational cost in mind, an SPH particle size of 0.075 mm was used for all walls, apart from the 0.7 mm thick corrugation walls where a particle size of 0.1 mm was applied. This gave between 5 and 7 SPH particles per wall thickness which was deemed enough to give a realistic energy transfer while keeping the computational cost within reason. The Lagrangian volume elements have a 0.05 mm element size through thickness and 0.2 mm in the in plane directions. The impactor has an SPH particle size of 0.075 mm, equal to that of the top facesheet.

Erosion is needed in all Lagrangian volume elements to remove distorted elements before they become degenerate. It can also be used to allow the simulation of material fracture, cutting and penetration. The higher the impact velocity, the higher the erosion strain recommended for use. For impacts up to 5 km/s, applying erosion at a geometric strain of 150% is common practice. At higher velocities, the geometric strain could reach 300% before the element should be eroded[24]. While erosion is not a physical process, if used with care it can lead to an accurate solution while preventing elements from becoming degenerate. In this set of simulations although the impact velocity is below 5 km/s, a high geometric strain of 500% is used on all volume elements

in order to minimize erosion.

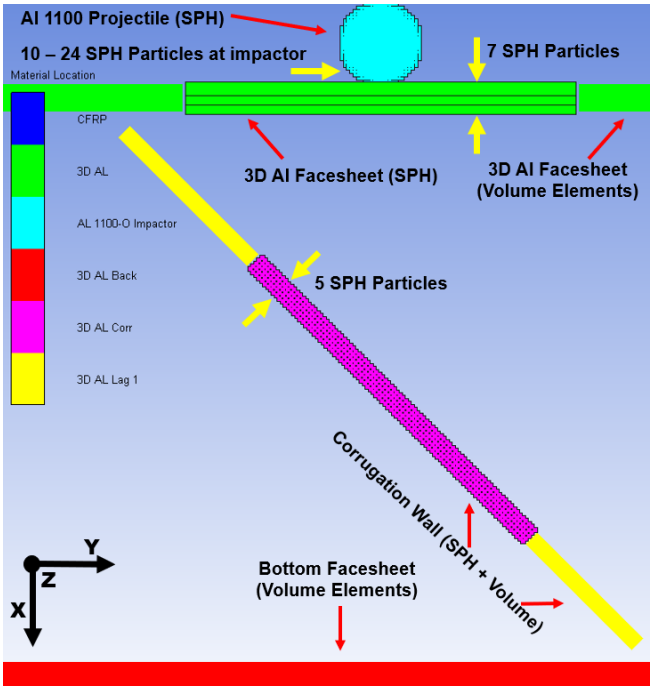

Figure 10: HVI model of the A03-01 single corrugated shield with a middle corrugation impact location. Z axis through page.

4.3.4 Material Models

The impactor is made up of Al 1100, a standard material whose HVI model can be found in the AUTODYN library. The shields are made up of 3D printed AlSi10Mg which is yet to be tested for detailed thermal and shock properties, especially at low wall thicknesses. Three major material inputs for the printed AlSi10Mg are needed: equation of state (EOS), strength model and failure model.

The EOS is needed to relate stress to deformation, internal energy and temperature. Strength gives the plasticity model that relates stress and strain. Failure is needed to recognize when tensile limits are reached to modify the computation to avoid unphysical solutions[25].

After a survey of the models available for EOS, strength and failure, the most appropriate combination was found to be a shock EOS, the Johnson Cook strength model and plastic strain failure. The actual inputs are a mix of contributions from the 3D printed AlSi10Mg material data sheet[14], the porosity models developed in [13] and impact data from previously tested isotropic Aluminium Alloys. These inputs are listed in Table 12 and one of the goals of this paper is to validate their use.

Equation of State	***Shock***
Reference Density	1.25 (g/cm^3)
Gruneisen coefficient	1.6 (none)
Parameter C1	3373 (m/s)
Parameter S1	1.3 (none)
Reference Temperature	293 (K)
Specific Heat	900 (J/kgK)
Failure Model	***Plastic Strain***
Plastic Strain	0.035 (none)
Strength Model	***Johnson Cook***
Shear Modulus	6.5385 e6 (kPa)
Yield Stress	2.5 e5 (kPa)
Hardening Constant	3 e5 (kPa)
Hardening Exponent	0.35 (none)
Strain Rate Constant	0.015 (none)
Thermal Softening Exponent	1 (none)
Melting Temperature	600 (K)
Ref. Strain Rate (/s)	1 (none)

Table 12: 3D Printed AlSi10Mg material properties used for the present set of HVI simulations

Note that [15] mentions a 10% average porosity level for the shields tested, while the model used and described in Table 12 uses properties scaled for 50% porosity. This is because the average porosity of the samples investigated in [13] is reliably obtained to be 50% based on Archimedes' method, while the areal densities reported in [15] require more analysis. It is agreed that porosity varies with wall thickness and that the porosity level found in [13] is accurate only for a thickness of 0.3 mm. However, the relation between print thickness and porosity level is unknown at the moment for AlSi10Mg and the present material model will be improved once this relation is obtained and different porosities can be applied for the 0.3 mm, 0.5 mm and 0.7 mm walls.

4.3.5 Results

As mentioned, for all corrugated shields three simulations were run, one for each impact location: corrugation top, middle and bottom. As a result, 18 3D HVI simulations were run in total: three for the baseline printed MSP samples and 15 for the corrugated shields. The total simulation time was 787 hours with five to six simulations running simultaneously at 50% efficiency on a Dell XPS 15 9560 with an Intel Core i7-7700 HQ CPU 2.8 GHz with 4 cores and 32 GB RAM.

The simulation results are presented in Table 13 in direct

comparison to the experimental outcome. The sample codes from Table 7 are used. Note that the simulation impact location reported in the table is the location that gave the overall closest results to the experimental data.

In terms of perforation, all simulated solutions have the same outcome as the experiments. This is especially relevant for the two unperforated samples (A04-01 and A08-01), because they are both close to their respective ballistic limits. For the other cases, the impact energy is easily high enough to break through the shields, and this does not necessarily point to a highly accurate simulation. In the case of A04-01 and A08-01 the other simulated impact locations (middle and bottom for A04-01 and top and middle for A08-01) do break through. This shows that the simulated model conveys accurately that the impact energy is around the ballistic limit of the shield. The simulations isolate the ballistic limit of these shields and they also prove a strong correlation between the impact location and the shield ballistic limit.

The front plate hole diameter is also consistent between experiments and simulations. On average, the difference between experiment and simulation is 0.49 mm which is only 11.55% of the average experimental hole size of 4.275 mm of the 8 samples in Table 13.

The back plate hole size is more difficult to assess because the holes are no longer circular and significant petalling occurs on some of the samples. The equivalent diameter of the hole is calculated by taking the square root of the product of the semi-minor and semi-major axis of the ellipse that circumscribes the hole. Perforation size is not the only important metric. Replicating the shape of the hole is also relevant and to that end the hole eccentricity is reported.

Looking at the samples that do not show petalling (A03-01, A03-02), the hole size difference is 0.98 mm on average with an average absolute experimental hole size of 10.1 mm. The average eccentricity difference is 0.08 for an average absolute experimental eccentricity of 0.945. As a result, the simulation is within 9.7% of the experiment in terms of back hole size and within 8.5% in terms of eccentricity. This shows a good correlation to the experimental data.

The samples with petalling stray significantly from the simulations in terms of hole size and shape. The simulations are stopped when the impactor energy has stabilized, which generally happens between 5 and 10 μs after the impact. Based on experimental photos, it takes more than 50 μs for petalling to occur, so it would be impossible to observe this additional deformation within a reasonable simulation time. Moreover, back plate volume elements with a geometric strain above 500% are eroded to avoid degeneration, so it even if the simulation would be run indefinitely petalling might not be observed. Finally, petalling tends to increase the eccentricity of the hole, which is reflected in the data since all petalled experimental samples have a higher eccentricity compared with the simulation. For the corrugated shields where impact location could be reported, the simulated representative impact location is accurate in two out of four cases. Note that in reality the impact does not occur exactly at one of the three locations investigated and the experimental observations had to be approximated.

Overall, the simulation technique together with the material model for 3D printed AlSi10Mg are validated through direct comparison to a set of 8 HVI experiments from the ReDSHIFT project. Most importantly, the material model for printed Aluminium can be used moving

Code	Sample Perforation (Yes/No)		Front Plate Hole Diameter (mm)		Back Plate Hole Equivalent Diameter (mm)		Back Plate Hole Eccentricity		Impact Location (Top/Mid/Bot)	
	Exp	Sim	Exp	Sim	Exp	Sim	Exp	Sim	Exp	Sim
A03-01	Yes	Yes	3.6	4	8.5	6.63	0.99	0.93	?	Top
A03-02	Yes	Yes	6	5.25	11.7	11.61	0.9	0.8	Top	Top
A04-01	No	No	4.3	4	N/A	N/A	N/A	N/A	Mid/Top	Bot
A05-01	Yes	Yes	2.8	3.5	11.7*	5.48	0.91	0.55	N/A	N/A
A06-01	Yes	Yes	3	3.75	?	1	0	0	N/A	N/A
A06-02	Yes	Yes	4.5	5	38.8*	10.4	0.74	0.66	N/A	N/A
A08-01	No	No	4.1	4	N/A	N/A	N/A	N/A	Bot	Bot
A09-02	Yes	Yes	5.9	5.75	27.9*	17.32	0.96	0.69	Top	Bot

Table 13: HVI simulation results. Numbers with an asterisk (*) pertain to samples with significant petalling on the back wall. Question marks are for numbers not available from experimental data.

forward to develop novel shield designs that can also undertake structural functions. Future testing to obtain more accurate shock properties for AlSi10Mg and other printed materials is still needed and more impact experimental samples from ReDSHIFT will be modelled, but this is a strong starting point.

5 RESULTS CONCLUSION

A summary of the relation between experimental results and theoretical/simulation predictions for the static loading cases is given in Table 14.

On average, for the SCP in bending, both theory and simulation predict a sample deflection around 29.5% less than the experimental value. Theory and simulation produce very similar results which gives confidence that sample performance on paper can be scaled reliably to predict experimental results.

In compression, both theory and simulation overpredict the experimental buckling load as they represent idealized versions of the real experiment. The theory assumes that corrugation members are built in, while the simulation similarly features perfect bonds between the struts. The theoretical buckling load is, on average, within 35% of the simulated value which shows reasonable agreement between the two idealized calculations.

In terms of compression sample stiffness, both theory and simulation significantly underpredict vertical displacement at failure. The relative movement of the experimental setup coupled with manufacturing faults in the printed shields lead to a much lower sample stiffness compared to the ideal cases. The positive aspect is that theory and simulation agree very well for S1C. This comparison is also reported in Table 14 and it shows that theory is within around 10% of the simulated value.

The HVI simulations are compared to the experimental results from five major points of view: sample perforation, front and back plate hole diameter, back hole eccentricity and predicted impact location. All five gave satisfactory results since the sample perforation is predicted correctly for all samples, the impact location is predicted well in two out of four cases, the front plate hole diameter is within 11.55% of the experimental value, the non-petalled back hole size is within 9.7% and the eccentricity within 8.5%. The material model used for AlSi10Mg is validated together with the computation technique and model setup used.

Overall, both theory and simulation replicate experimental results well and give a robust set of idealized data that can be later developed and extrapolated for novel designs. While sample porosity is accounted for in the values of Young's modulus and shear modulus, a better understanding regarding the effect of porosity on the effective load bearing thickness of the printed shield walls is needed together with a relation between wall thickness and porosity level.

Sample	Theoretical Values	Simulation Values
S1B	$\Delta y_{th} = 0.7177 \times \Delta y_{exp}$	$\Delta y_{sim} = 0.6952 \times \Delta y_{exp}$
S1C	$\Delta y_{th} = 0.0446 \times \Delta y_{exp}$ $\Delta y_{th} = 0.888 \times \Delta y_{sim}$ $F_{th} = 2.3744 \times F_{exp}$	$\Delta y_{sim} = 0.05 \times \Delta y_{exp}$ $F_{sim} = 3.65 \times F_{exp}$

Table 14: Theoretical and simulation results comparison to experimental data

To conclude, this investigation provides insight into the structural and shielding performance of 3D printed corrugated orbital debris shields through direct comparison to both standard and printed CFRP Al honeycomb cores. In both bending and compression the shields perform worse than either honeycomb which underlines the compromise that may have to be made when integrating shields with spacecraft primary structures. Moreover, the shielding performance of the printed corrugations is explored and it is underlined that corrugated shields generally perform similarly or slightly outperform similar areal density printed MSPs. A material model for AlSi10Mg and a simulation method are proposed and validated for further use, with the caveat that when data becomes available the material model should be changed for each wall thickness. Real life shock testing for the printed material is also needed for more accurate simulation solutions, while manufacturing inconsistencies and sample defects need to be addressed to obtain consistent prints of valuable structural and shielding performance.

Acknowledgements

The experimental work reported was funded through the European Commission Horizon 2020, Framework Programme for Research and Innovation (2014-2020), under the ReDSHIFT project (grant agreement n. 687500).

6 References

[1] Whipple F.L. *Meteorites and space travel. AJ*, 52:131, 1947.

[2] Cour-Palais B. *Meteoroid protection by multiwall structures.* In *Hypervelocity Impact Conference*, page 372, 1969.

[3] Christiansen E. *Advanced meteoroid and debris shielding concepts.* In *Orbital Debris Conference: Technical Issues and Future Directions*, page 1336, 1990.

[4] Christiansen E.L. *Design and performance equations for advanced meteoroid and debris shields. International Journal of Impact Engineering*, 14(1-4):145–156, 1993.

[5] Christiansen E.L. and Kerr J.H. *Ballistic limit equations for spacecraft shielding. International Journal of Impact Engineering*, 26(1-10):93–104, 2001.

[6] Schonberg W.P. and Tullos J.R. *Spacecraft wall design for increased protection against penetration by orbital debris impacts. AIAA journal*, 29(12):2207–2214, 1991.

[7] Zhou H., Guo R., and Liu R. *Protection properties of stuffed corrugated sandwich structures under hypervelocity impact: Numerical simulation. Journal of Sandwich Structures & Materials*, 21(2):532–551, 2019.

[8] Reimerdes H.G., Noelke D., and Schäfer F. *Modified Cour-Palais/Christiansen damage equations for double-wall structures. International journal of impact engineering*, 33(1-12):645–654, 2006.

[9] Taylor E.A., Herbert M.K., Vaughan B.A.M., and McDonnell J.A.M. *Hypervelocity impact on carbon fibre reinforced plastic/aluminium honeycomb: comparison with Whipple bumper shields. International Journal of Impact Engineering*, 23(1):883–893, 1999.

[10] Kinslow R. and Gehring J. W. *High-velocity impact phenomena, Chapter IX: Engineering Considerations.* Elsevier, 1970.

[11] Jex D.W., Mac Kay C.A., and Miller A.M. *The characteristics of penetration for a double-sheet structure with honeycomb.* 1970.

[12] Revolutionary Design of Spacecraft through Holistic Integration of Future Technologies. `https://cordis.europa.eu/project/id/687500`, Jan 2016.

[13] Dumitrescu A., Walker S.J.I., Romei F., and Bahaskar A. *The structural assessment of sandwich panels with 3D printed cores for spacecraft applications.* In *European Conference on Spacecraft Structures, Materials and Environmental Testing (ECSSMET)*, 2021.

[14] Olivieri L., Giacomuzzo C., Sarego G., and Francesconi A. *ReDSHIFT - 3D Printing Design Strategy.* Technical report, 2019.

[15] Olivieri L., Giacomuzzo C., Francesconi A., Geradin S., Bagatin M., Paccagnella A., Finozzi A., Stokes H., Romei F., Walker S.J.I., et al. *Experimental characterization of multi-layer 3D-printed shields for microsatellites, Paper IAC-18, A6, 3, 7.* In *69th International Astronautical Congress (IAC), Bremen, Germany*, pages 1–5, 2018.

[16] Romei F., Rumpf C., and Walker S.J.I. *ReDSHIFT - Hypervelocity Impact Test Analysis.* Technical report, 2019.

[17] Valdevit L., Hutchinson J.W., and Evans A.G. *Structurally optimized sandwich panels with prismatic cores. International Journal of Solids and Structures*, 41(18-19):5105–5124, 2004.

[18] Valdevit L., Wei Z., Mercer C., Zok F.W., and Evans A.G. *Structural performance of near-optimal sandwich panels with corrugated cores. International Journal of Solids and Structures*, 43(16):4888–4905, 2006.

[19] Cedolin L. et al. *Stability of structures: elastic, inelastic, fracture and damage theories.* World Scientific, 2010.

[20] Côté F., Deshpande V.S., Fleck N.A., and Evans A.G. *The compressive and shear responses of corrugated and diamond lattice materials. International Journal of Solids and Structures*, 43(20):6220–6242, 2006.

[21] Shanley F.R. *Inelastic column theory. Journal of the aeronautical sciences*, 14(5):261–268, 1947.

[22] Zhou H., Guo R., and Liu R. *Protection properties of stuffed corrugated sandwich structures under hypervelocity impact: Numerical simulation. Journal of Sandwich Structures & Materials*, 21(2):532–551, 2019.

[23] Wicklein M., Ryan S., White D.M., and Clegg R.A. *Hypervelocity impact on CFRP: testing, material modelling, and numerical simulation. International Journal of Impact Engineering*, 35(12):1861–1869, 2008.

[24] Hayhurst C.J., Ranson H.J., Gardner D.J., and Birnbaum N.K. *Modelling of microparticle hypervelocity oblique impacts on thick targets. International journal of impact engineering*, 17(1-3):375–386, 1995.

[25] ANSYS. *Explicit Dynamics Analysis Guide*, 2019.